

# Sub-Monolayer $YO_x/MoO_x$ on Ultrathin Pt Nanowires Boosts Alcohol Oxidation Electrocatalysis

Menggang Li, Zhonglong Zhao, Weiyu Zhang, Mingchuan Luo, Lu Tao, Yingjun Sun, Zhonghong Xia, Yuguang Chao, Kun Yin, Qinghua Zhang, Lin Gu, Weiwei Yang, Yongsheng Yu,\* Gang Lu,\* and Shaojun Guo\*

A crucial issue restricting the application of direct alcohol fuel cells (DAFCs) is the low activity of Pt-based electrocatalysts for alcohol oxidation reaction caused by the reaction intermediate (CO\*) poisoning. Herein, a new strategy is demonstrated for making a class of sub-monolayer YO<sub>x</sub>/MoO<sub>x</sub>-surface codecorated ultrathin platinum nanowires (YOx/MoOx-Pt NWs) to effectively eliminate the CO poisoning for enhancing methanol oxidation electrocatalysis. By adjusting the amounts of YO, and MoO, decorated on the surface of ultrathin Pt NWs, the optimized 22% YO,/MoO,-Pt NWs achieve a high specific activity of 3.35 mA cm<sup>-2</sup> and a mass activity of 2.10 A mg<sub>pt</sub><sup>-1</sup>, as well as the enhanced stability. In situ Fourier transform infrared (FTIR) spectroscopy and CO stripping studies confirm the contribution of YO<sub>x</sub> and MoO<sub>y</sub> to anti-CO poisoning ability of the NWs. Density functional theory (DFT) calculations further reveal that the surface Y and Mo atoms with oxidation states allow COOH\* to bind the surface through both the carbon and oxygen atoms, which can lower the free energy barriers for the oxidation of CO\* into COOH\*. The optimal NWs also show the superior activities toward the electro-oxidation of ethanol, ethylene glycol, and glycerol.

1. Introduction

The depleting fossil fuel and increasing environmental pollution have motivated the development of electrochemical-process-based renewable energy technologies.<sup>[1–3]</sup> The direct

alcohol fuel cells (DAFCs) attract wide attentions due to their high energy density, environmental insensitivity, and low operating temperature, etc.[3-5] To enable the widespread application of this technology, anodic catalysts with high efficiency and stability are required to drive the alcohol oxidation reactions. [6-8] To date, platinum (Pt) is still the state-of-the-art anodic electrocatalysts in DAFCs.[9-13] However, pure Pt catalysts with high cost show the sluggish reaction kinetic and strong CO poisoning problems.[14-18] To address these issues, an efficient strategy is to combine Pt and other metals (such as Ni, Cu, Fe, and Ga) to form stable bimetallic or trimetallic alloys.[19-26] By further precisely designing the nanostructures of Pt-based catalysts with tailored sizes, dimensions, morphologies, or compositions, the welldesigned Pt-based alloys can not only reduce the consumption of Pt, but also achieve considerably enhanced activities.

Especially, the ultrathin structure (generally <2 nm) can expose more surface active sites to achieve the high utilization of Pt atoms, which is thus considered to be an ideal platform for boosting electrocatalytic activity. Even though significantly high activities have been realized, these conventional ultrathin

M. Li, W. Yang, Y. Yu MIIT Key Laboratory of Critical Materials Technology for New Energy Conversion and Storage School of Chemistry and Chemical Engineering Harbin Institute of Technology Harbin, Heilongjiang 150001, China E-mail: ysyu@hit.edu.cn

M. Li, W. Zhang, M. Luo, L. Tao, Y. Sun, Z. Xia, Y. Chao, K. Yin, S. Guo School of Materials Science and Engineering

Peking University
Beijing 100871, China
E-mail: guosj@pku.edu.cn
Z. Zhao

School of Physical Science and Technology Inner Mongolia University Hohhot 010021, China

The ORCID identification number(s) for the author(s) of this article can be found under https://doi.org/10.1002/adma.202103762.

DOI: 10.1002/adma.202103762

Z. Zhao, G. Lu
Department of Physics and Astronomy
California State University Northridge
Northridge, CA 91330, USA
E-mail: ganglu@csun.edu

Q. Zhang, L. Gu Beijing National Laboratory for Condensed Matter Physics Institute of Physics Chinese Academy of Sciences Beijing 100190, China S. Guo

BIC-ESAT College of Engineering Peking University Beijing 100871, China



www.advancedsciencenews.com



www.advmat.de

Pt-based catalysts tend to catalyze the oxidation of alcohol molecules to generate adsorbed CO intermediates (CO\*) and form strong Pt–CO\* bonds, making the poisoning CO\* be difficult to desorb from the surface. [36–41] This annoying reaction intermediate inhibits the overall oxidation from alcohol to CO<sub>2</sub>. The introduction of oxophilic metals, including Mo, Ru, and Rh, has been proven a good way for alleviating the CO poisoning because they are easier to generate the adsorbed hydroxyl group (OH<sub>ads</sub>) at lower potential. [14,25,41–46] Despite much progress has been made in the functional mechanism of Pt-based alloy catalysts, exploring a new catalyst system for restricting the CO poisoning issue is still a grand challenge till date.

Considering rare earth metals with unique electronic structure may provide a new platform for improving the electrocatalytic performance of noble metals, herein, we report a class of sub-monolayer YO<sub>x</sub>/MoO<sub>x</sub> on ultrathin Pt nanowires (YO<sub>x</sub>/MoO<sub>x</sub>-Pt NWs) for alleviating the CO poisoning and enhancing the alcohol oxidation. Different from the traditional Pt and Pt alloy catalysts, in this catalytic system, we find that YO<sub>x</sub>/MoO<sub>x</sub>-Pt NWs can achieve a new decoupling process for restricting the CO poisoning, in which the free energy of CO\* and COOH\* can be decoupled on the surface of YO<sub>x</sub>/MoO<sub>x</sub>-Pt NWs. We have demonstrated that the optimal 22% YO<sub>x</sub>/MoO<sub>x</sub>-Pt NWs have the specific activity of 3.35 mA cm<sup>-2</sup> and the mass activity of 2.10 A mg<sub>Pt</sub><sup>-1</sup>, respectively, for methanol oxidation reaction (MOR), ≈2.21 and ≈3.75 times higher than those of the commercial Pt/C. In situ Fourier transform infrared (FTIR) spectroscopies reveal that the decoration of YO<sub>x</sub>/MoO<sub>x</sub> can induce the CO\* thermodynamically transferred from linear mode (CO<sub>1</sub>) to bridge mode (CO<sub>B</sub>), lowering the barrier of the further oxidation. The CO stripping results further demonstrate the contribution of YOx/MoOx to anti-CO poisoning. The significant enhanced catalytic activities can be further extended to the electro-oxidation of various polyalcohols, including the ethanol, ethylene glycol, and glycerol.

# 2. Results and Discussion

The YO<sub>x</sub>/MoO<sub>x</sub>-Pt NWs were synthesized by the use of Pt(acac)<sub>2</sub>, Y(acac)<sub>3</sub>, and Mo(CO)<sub>6</sub> as metal precursors (see the Supporting Information for details), and Mo(CO)6 and cetyltrimethylammonium bromide (CTAB) as the structuredirecting agents. The transmission electron microscopy (TEM) (Figure 1a,c) and high-angle annular dark-field scanning transmission electron microscopy (HAADF-STEM) (Figure 1b) images show that the products have ultrathin nanowire structure with the uniform diameter of 1.2  $\pm$  0.2 nm and the length of 40  $\pm$  20 nm, respectively (Figure 1d; Figure S1, Supporting Information). The atomic ratio of Y/Mo/Pt in these NWs is estimated to be 8/14/78 according to the scanning electron microscopy-energy-dispersive X-ray spectroscopy (SEM-EDS) result, being consistent with the inductively coupled plasma-atomic emission spectroscopy (ICP-AES) (Figure S2, Supporting Information). The atomic-resolution aberration-corrected highresolution HAADF-STEM image (Figure 1e) further reveals the ultrathin structure with six or seven atomic layers. Obviously, the NWs are composed of atoms with different brightness, where dark dots (representing Y or Mo atoms, marked

by purple arrows) are rich in the edge of the NWs, and bright dots (representing Pt atoms, marked by green boxes) appear mainly in a more central position. Therefore, the surface of assynthesized ultrathin NWs is enriched by sub-monolayer Y and Mo atoms. However, we can observe the homogeneous distribution of Pt, Y, and Mo throughout the whole ultrathin NWs from the STEM-EDS mapping (Figure S3, Supporting Information). This is because the bright Pt atoms can cover the dark Y or Mo atoms in the bulk phase of NWs. In addition, the wellorganized polycrystallized structure can be obviously observed on the NWs, confirmed by the selected-area electron diffraction (SAED) and corresponding selected-area fast Fourier transform (FFT) patterns (the inset of Figure 1e; Figure S4, Supporting Information). Figure 1f, the enlarged red area of Figure 1e, shows the lattice spacings of 0.223 and 0.191 nm, corresponding to the (111) and (200) facets of a typical face-centered cubic (fcc) structure of Pt, whereas Figure 1g, the enlarged orange area of Figure 1e, shows the lattice spacing of 0.223 nm, attributed to the (111) facet of fcc Pt. Their corresponding selected-area FFT patterns (the right parts of Figure 1f,g) demonstrate the typical [110] and [-112] zones of diffraction.

X-ray photoelectron spectroscopy (XPS) analysis (Figure S5, Supporting Information) further verifies the co-existence of Pt, Y, and Mo in the as-prepared NWs. Moreover, the high-resolution XPS spectra of Pt, Y, and Mo are further deconvoluted to examine the chemical states in the NWs (Figure 1h-j). Obviously, the dominating Pt atoms are mainly in the metallic state. However, both Y and Mo atoms in the NWs exist in the form of oxidation states. Therefore, we here denoted them as the YO<sub>x</sub> and MoOx, respectively. By changing the feeding amount of Y(acac)<sub>3</sub>, various ultrathin Pt-based NWs with similar sizes but different composition can be obtained (Figures S6 and S7, Supporting Information). In the powder X-ray diffraction (PXRD) patterns (Figure 1k), all the NWs show the fcc structure of Pt (JCPDS No. 04-0802), and no obvious peaks for the Y- or Mobased structure can be observed, indicating that the YO<sub>x</sub> and  $MoO_x$  are in the form of amorphous oxide. The similar metal atomic ratios, determined by the XPS, SEM-EDS, and ICP-AES, further confirm the ultrathin structures of all NWs (Table S1, Supporting Information). Taking into account the metal atomic ratios, herein we define them as 5%  $MoO_x$ -Pt, 14%  $YO_x/MoO_x$ -Pt, 22% YO<sub>x</sub>/MoO<sub>x</sub>–Pt, and 27% YO<sub>x</sub>/MoO<sub>x</sub>–Pt, respectively.

The growth mechanism of sub-monolayer YO<sub>x</sub>/MoO<sub>x</sub>surface co-decorated ultrathin Pt NWs was revealed by characterizing the intermediates collected at different reaction stages (Figures S8-S11, Supporting Information). We found that the NWs' evolution was controlled by the oriented attachment and the Ostwald ripening process, mainly involving three stages, i.e., the initial reduction of Pt nanoparticles (NPs), further growth of oxidized Mo species-decorated ultralong Pt NWs, and the final formation of YO<sub>x</sub>/MoO<sub>x</sub> co-decorated ultrathin Pt NWs (Figure S12, Supporting Information). In this wet-chemical synthesis system, the feeding of CTAB is crucial to form the 1D NWs, in which the CTA+ plays the structure-directing role instead of Br- (Figures S13-S15, Supporting Information). In addition, the carbonyl group decomposed from the Mo(CO)<sub>6</sub> is also a necessity for making ultrathin NWs, and the amount of Mo(CO)<sub>6</sub> strongly restricts the uniformity of NWs (Figures S16-S19, Supporting Information).

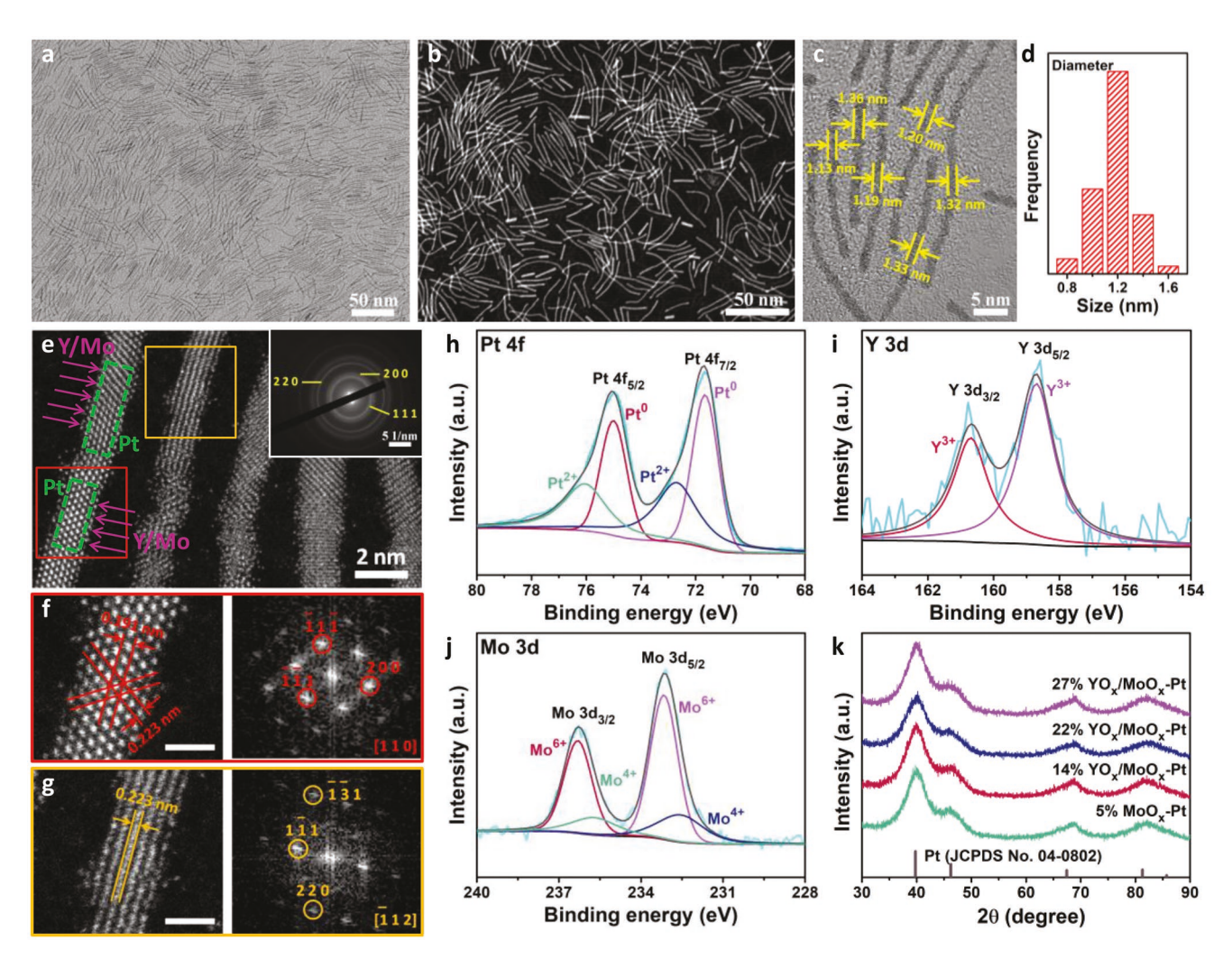


**Figure 1.** Structural and compositional characterizations of sub-monolayer YO<sub>x</sub>/MoO<sub>x</sub>-surface co-decorated ultrathin Pt NWs. a—e) Representative low-magnification (a) and high-magnification (c) TEM images, b) HAADF-STEM image, d) histogram of diameter distribution, and e) atomic-resolution HAADF-STEM image (inset is the corresponding SAED pattern) of 22% YO<sub>x</sub>/MoO<sub>x</sub>–Pt NWs. f,g) The enlarged atomic-resolution HAADF-STEM images and corresponding FFT patterns taken from red square and orange square in (e), respectively (the scale bars are 1 nm). h—j) High-resolution XPS spectra of Pt 4f (h), Mo 3d (i), and Y 3d (j) in 22% YO<sub>x</sub>/MoO<sub>x</sub>–Pt NWs. k) PXRD patterns of different NWs.

sub-monolayer  $YO_x/MoO_x$ -surface-co-decorated ultrathin Pt NWs were explored as electrocatalysts for alcohol oxidation. The NWs were loaded onto the Ketjen Black-300J via sonicating, followed by treating with an acetic acid solution to remove organic molecules on the surface of NWs (Figure S20, Supporting Information). According to the cyclic voltammograms (CVs) (Figure 2a), the electrochemically active surface areas (ECSAs) are determined to be 51.5, 56.4, 62.7, and 58.2 m<sup>2</sup> g<sup>-1</sup> for 5% MoO<sub>x</sub>-Pt, 14% YO<sub>x</sub>/MoO<sub>x</sub>-Pt, 22% YO<sub>x</sub>/MoO<sub>x</sub>-Pt, and 27% YO<sub>x</sub>/MoO<sub>x</sub>-Pt, respectively, very close to that of commercial Pt/C (54.3 m<sup>2</sup> g<sup>-1</sup>). Furthermore, the current densities are further normalized by the Pt mass (Figure 2b) and ECSAs (Figure S21, Supporting Information) to evaluate the MOR activities. The anodic peak current density follows the order of  $22\% \text{ YO}_x/\text{MoO}_x-\text{Pt} > 27\% \text{ YO}_x/\text{MoO}_x-\text{Pt} > 14\% \text{ YO}_x/\text{MoO}_x-$ Pt > 5%  $MoO_x$ -Pt > Pt/C. Specifically, the optimal 22%  $YO_x$ / MoO<sub>x</sub>-Pt achieves a high specific activity of 3.35 mA cm<sup>-2</sup> and a high mass activity of 2.10 A mg<sub>Pt</sub><sup>-1</sup>, exceeding those of commercial Pt/C by 2.21 and 3.75 times, respectively (Figure 2c).

The mass activity of 22%  $YO_x/MoO_x$ -Pt is the best in all the reported state-of-the-art catalysts (Table S2, Supporting Information). The onset potentials of as-obtained YOx/MoOx-Pt catalysts (including 14% YO<sub>x</sub>/MoO<sub>x</sub>-Pt, 22% YO<sub>x</sub>/MoO<sub>x</sub>-Pt, and 27% YO<sub>x</sub>/MoO<sub>x</sub>-Pt) are all shifted negatively by around 30 and 70 mV compared to those of 5% MoO<sub>x</sub>-Pt and commercial Pt/C, respectively (Figure 2d). This confirms the faster reaction kinetics of YO<sub>x</sub>/MoO<sub>x</sub>-Pt for MOR. In addition, the ratio of the forward current  $(I_f)$  to the reverse current  $(I_h)$  of 22% YO<sub>x</sub>/MoO<sub>x</sub>-Pt is calculated to be 1.14, larger than those of 5% MoO<sub>x</sub>-Pt (1.00) and commercial Pt/C (0.92) (Figure 2e; Table S3, Supporting Information), indicating its higher tolerance to CO poisoning intermediates due to the YO<sub>x</sub> and MoO<sub>x</sub> species' decoration. In addition, the enhanced MOR activity caused by the YOx and MoOx species' decoration was also found in Pt NP system (Figures S22 and S23, Supporting Information).

The stability of these catalysts toward MOR was further assessed by applying consecutive potential cycles at a scan rate

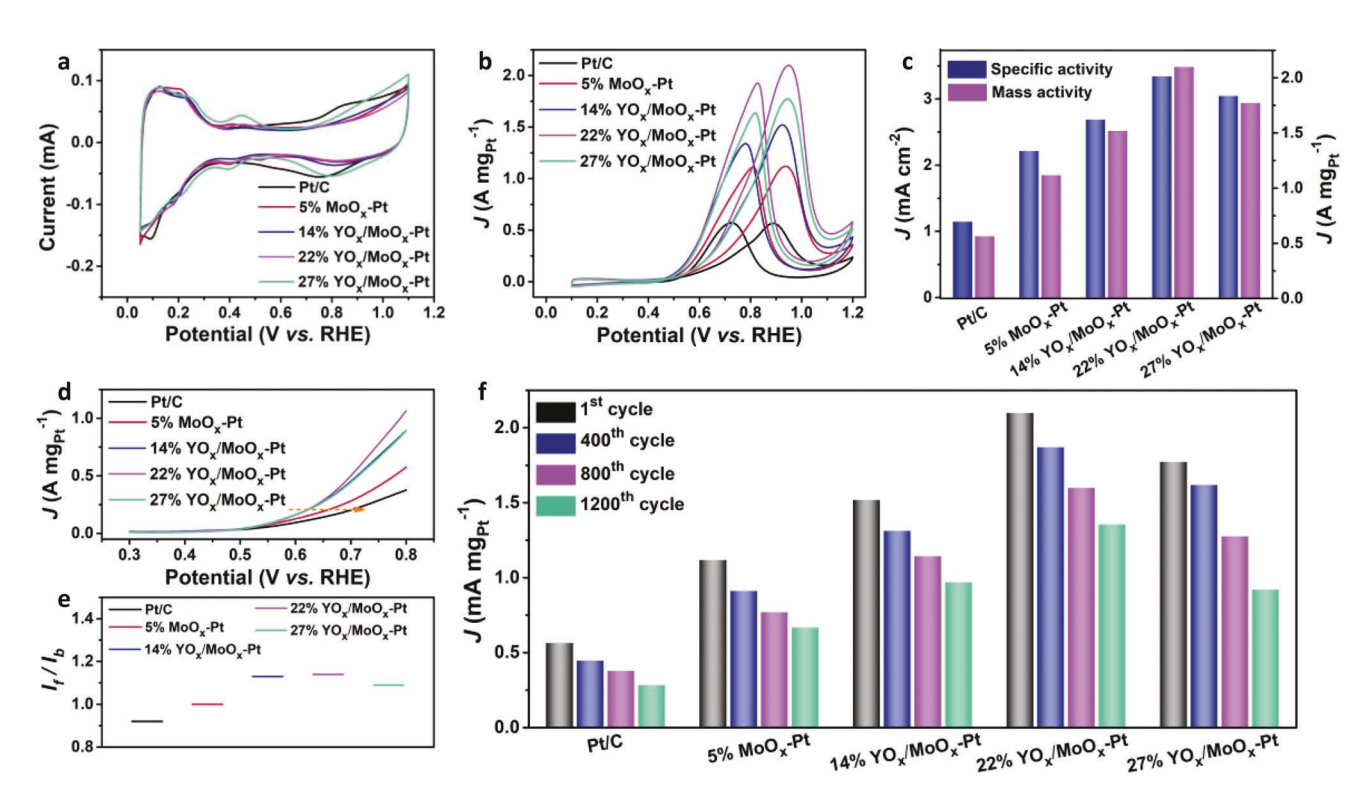


Figure 2. Electrocatalytic MOR performance on different catalysts. a) CVs, b) Pt mass-normalized MOR, c) comparison on the specific activities and mass activities, d) linear sweep voltammogram (LSV) curves, e) the  $I_f/I_b$  ratios derived from the MOR, and f) mass activities after different scan cycles.

of 50 mV s<sup>-1</sup> (Figure S24, Supporting Information). As shown in Figure 2f, the 22% YO<sub>x</sub>/MoO<sub>x</sub>–Pt can still maintain a high mass activity of 1.36 A mg<sub>Pt</sub><sup>-1</sup> after 1200 cycles, retaining 64.7% of the initial value, much higher than those of 5% MoO<sub>x</sub>-Pt (59.8%) and commercial Pt/C (50.6%). Chronoamperometric (CA) tests show that the current density of 22% YO<sub>x</sub>/MoO<sub>x</sub>-Pt after 3000 s is still higher than those of the other catalysts (Figure S25, Supporting Information). In addition, the 22% YOx/MoOx-Pt and 5% MoO<sub>x</sub>-Pt ultrathin nanowires were well preserved after the stability test, while the commercial Pt/C exhibited severe aggregation under the same condition (Figure S26, Supporting Information). Furthermore, the negligible compositional decrease further confirms the excellent stability (Figure S27, Supporting Information). The high MOR stability of YOx/MoOx-Pt nanowires is probably caused by their unique 1D composite structure, in which they can not only provide strong interaction between them and carbon support, thus maintaining a well structural stability, but also effectively restrict the CO poisoning issue during the long-term MOR tests.

In order to gain insightful understanding of the enhanced MOR performance on the  $YO_x/MoO_x$ –Pt, we employed the in situ FTIR spectroscopy on the 22%  $YO_x/MoO_x$ –Pt and commercial Pt/C catalysts (**Figure 3**a–d; Figure S28, Supporting Information). Several bands between 2500 and 1000 cm<sup>-1</sup> can be observed clearly in the investigated potential window. The downward bands at 2341 cm<sup>-1</sup> can be attributed to the asymmetric stretch vibration of  $CO_2$ . [47,48] The  $CO_2$  is the final product of methanol oxidation, reflecting the completing oxidation of methanol. The bipolar bands near 2010 cm<sup>-1</sup> can be assigned to the linear-absorbed CO ( $CO_1$ ). [49,50] The downward peaks at

around 1810 cm<sup>-1</sup> indicate the bridge-absorbed CO (CO<sub>R</sub>).<sup>[51–53]</sup> It is displayed explicitly that CO<sub>2</sub> appears at a much lower potential in the FTIR spectra of 22% YO<sub>x</sub>/MoO<sub>x</sub>-Pt (0.40 V) than that of commercial Pt/C (0.60 V), manifesting the easier completing oxidation of methanol on the 22% YO<sub>x</sub>/MoO<sub>x</sub>-Pt. Both of CO<sub>1</sub> and CO<sub>B</sub> absorbed on the 22% YO<sub>x</sub>/MoO<sub>x</sub>-Pt are detected via in situ FTIR spectroscopy at low potential (≈0.20 V), and then the peaks disappear with increasing the potential. However, only CO<sub>L</sub> can be monitored during the MOR process on commercial Pt/C from 0.20 V, and cannot be removed at high potential. In addition, the CO stripping experiments were carried out to reveal the anti-CO poisoning ability of YO<sub>x</sub>/MoO<sub>x</sub>-Pt NWs (Figure 3e). Compared with the commercial Pt/C and 5%  $MoO_x$ -Pt, the CO onset oxidation potential of 22%  $YO_x$ / MoO<sub>x</sub>-Pt shows the negative shifts of 88 and 75 mV, respectively. Combining the FTIR and CO stripping studies, it can be concluded that the 22% YOx/MoOx-Pt possesses higher anti-CO poisoning property.

Density functional theory (DFT) calculations were performed to elucidate the origin of enhanced MOR activities on the sub-monolayer  $YO_x/MoO_x$  surface-co-decorated ultrathin Pt NWs. We constructed a pure Pt (111) slab model, and replaced one of the Pt atoms on the surface with Mo to represent the oxidized Mo species-decorated structure. And in the oxidized Y, Mo species-co-decorated model, one more surface Pt atom is replaced by a Y atom. We find that the Y and Mo atoms on the surface tend to avoid each other (Figure S29, Supporting Information). Therefore, it should be difficult for a reaction intermediate to occupy both of the surface Y and Mo sites simultaneously.

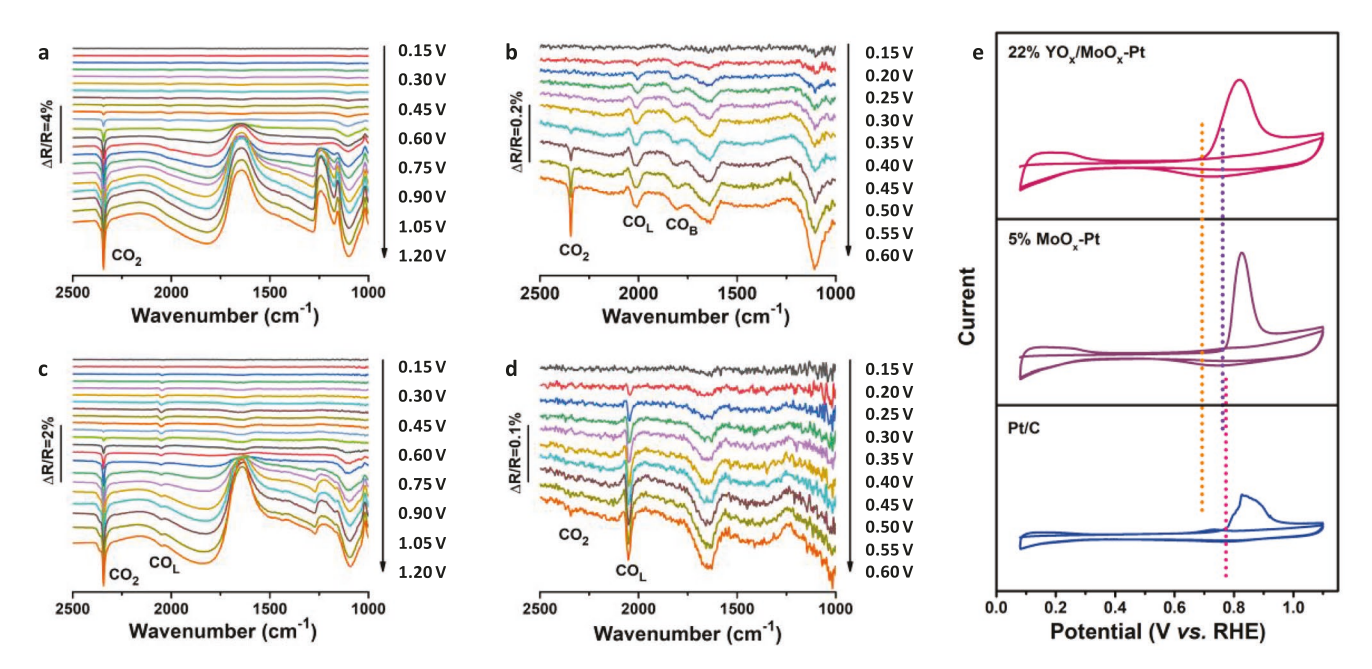


Figure 3. In situ FTIR spectra and CO stripping curves of different catalysts. a) In situ FTIR spectra recorded from 0.15 to 1.20 V versus reversible hydrogen electrode (RHE) and b) magnified in situ FTIR spectra recorded from 0.15 to 0.60 V versus RHE during MOR on 22%  $YO_x/MoO_x$ –Pt. c) In situ FTIR spectra recorded from 0.15 to 1.20 V versus RHE and d) magnified in situ FTIR spectra recorded from 0.15 to 0.60 V versus RHE during MOR on commercial Pt/C. The reference potential is 0.1 V versus RHE. e) CO stripping curves of 22%  $YO_x/MoO_x$ –Pt, 5%  $MoO_x$ –Pt, and commercial Pt/C.

As is known, Pt nanomaterials can be served as the active MOR catalysts.  $^{[54,55]}$  However, those of the pure Pt nanocatalysts suffer from the poisoning of CO\* (\* indicates adsorbed species), which is a typical intermediate in the reaction pathway, thus, deactivating the active surface sites during the MOR. [56,57] Therefore, we simulated the free energy changes for the CO\* desorption on the pure Pt, MoO<sub>x</sub>-Pt, and YO<sub>x</sub>/MoO<sub>x</sub>-Pt surfaces (Figure 4a). We find that CO\* tends to bind to the surface Pt sites (instead of the Y and Mo sites) in an upright geometry concerning the C atom. CO\* poisoning, as a result, will deactivate all three surfaces just like that on a pure Pt surface. The desorption of CO\* on the pure Pt, MoO<sub>x</sub>-Pt, and YO<sub>x</sub>/MoO<sub>x</sub>-Pt surfaces requires a very high energy input, which are calculated as 1.00, 0.97, and 0.92 eV, respectively. On the other hand, the oxidation of CO\* into COOH\* intermediate on the pure Pt surface also requires a high free energy input of 0.98 eV (Figure 4b), making the overall oxidation unattainable.

We attribute the enhanced MOR activities on the ultrathin  $YO_x/MoO_x$ –Pt NWs to a decoupling mechanism between the CO\* and COOH\* intermediates (Figure 4c,d). In contrast to the upright geometry of CO\* on the surface, the COOH\* tends to bind to the surface in a planar geometry with respect to both of the C and O atoms. Due to the higher oxygen affinity of Mo and Y compared with that of Pt, the free energy of COOH\* can be lowered in terms of the Mo–O or Y–O interaction without affecting the free energy of CO\*. Therefore, the free energies of CO\* and COOH\* are decoupled on the  $YO_x/MoO_x$ –Pt surfaces. However, such a decoupling mechanism cannot be achieved on a pure Pt surface. As shown in Figure 4b, the free energy for the oxidation of CO\* into COOH\* on the  $MoO_x$ –Pt and  $YO_x/MoO_x$ –Pt can be lowered to 0.64 and 0.20 eV, respectively. On this mechanism, we can simply attribute the higher MOR

activity of the  $YO_x/MoO_x$ -Pt to the higher oxygen affinity of Y compared with Mo on the surface.

The full-reaction free energy diagram for MOR on the YO<sub>x</sub>/ MoO<sub>x</sub>-Pt surface was studied by examining the following plausible intermediates: OCH3\*, CH2OH\*, CH2O\*, CHOH\*, COH\*, CHO\*, CO\*, and COOH\* (Figure 4e; Figure S30, Supporting Information). The oxidation can proceed on the YO<sub>x</sub>/ MoO<sub>x</sub>-Pt surface through the reaction pathway CH<sub>3</sub>OH →  $CH_2OH^* \,\rightarrow\, CH_2O^* \,\rightarrow\, CHO^* \,\rightarrow\, CO^* \,\rightarrow\, COOH^* \,\rightarrow\, CO_2,$ overlapping partially with the MOR pathway on the pure Pt surface, but deviates from it at the oxidation of CH2OH\*. CH2OH\* is oxidized to CH<sub>2</sub>O\* and then to CHO\* on the YO<sub>x</sub>/MoO<sub>x</sub>-Pt surface, while on the pure Pt surface, CH2OH\* is oxidized to CHOH\*, followed by a COH\* intermediate. After that, the reaction pathways overlap again. Due to the decrease of the relative free energy of COOH\*, the final oxidation of COOH\* to CO<sub>2</sub> becomes the overpotential-determining step for MOR on the  $YO_x/MoO_x$ -Pt NWs. The MOR overpotential on the  $YO_x/MoO_x$ -Pt NWs. MoO<sub>x</sub>-Pt surface is calculated as 0.44 V, 55% lower than that on the pure Pt surface (1.00 V), on which the overpotential-determining step is still the oxidation of CO\* to COOH\*.

We further studied the ethanol oxidation reaction (EOR), ethylene glycol oxidation reaction (EGOR), and glycerol oxidation reaction (GOR) performances of these catalysts. The activity of EOR follows the similar trend to that of MOR: 22%  $YO_x/MoO_x$ –Pt > 27%  $YO_x/MoO_x$ –Pt > 14%  $YO_x/MoO_x$ –Pt > 5%  $MoO_x$ –Pt > Pt/C (**Figure 5a**; Figure S31, Supporting Information). As shown in Figure 5b, the 22%  $YO_x/MoO_x$ –Pt features a specific activity of 2.59 mA cm<sup>-2</sup> and a mass activity of 1.63 A  $mg_{Pt}^{-1}$ , much higher than those of the NW catalysts with other compositions, commercial Pt/C, and most of previously state-of-theart electrocatalysts (Table S4, Supporting Information). The  $I_f/I_b$ 

www.advancedsciencenews.com

www.advmat.de

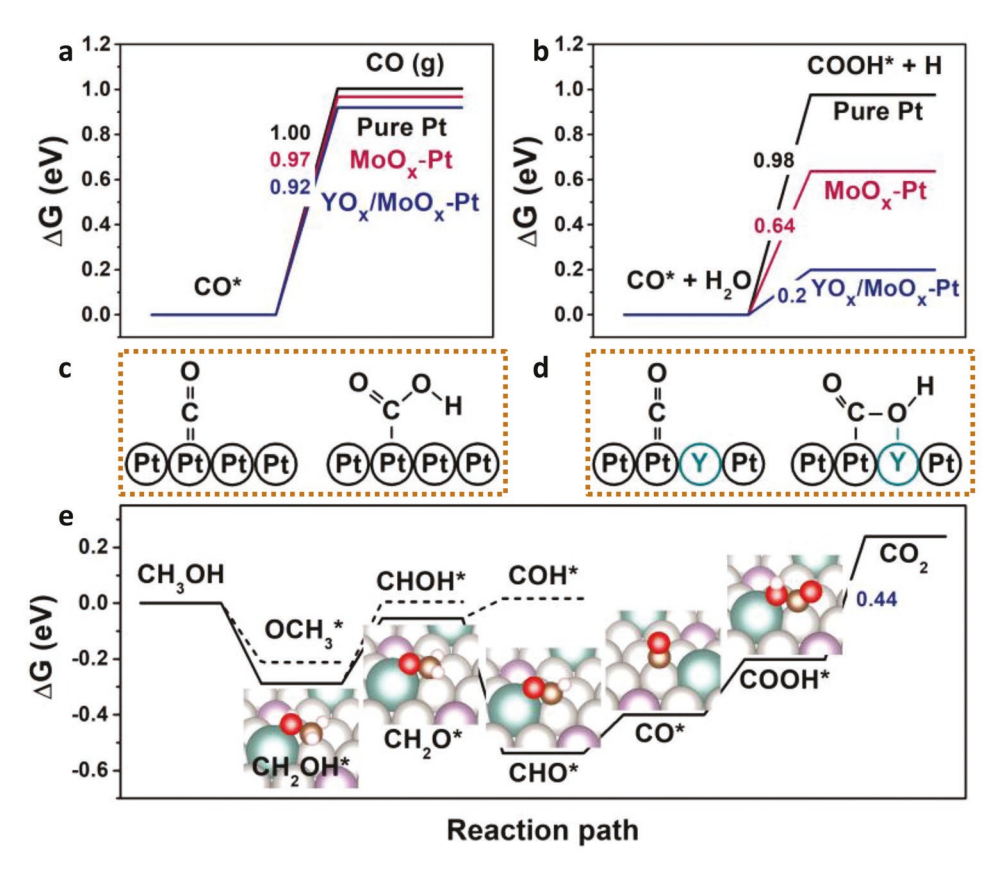


Figure 4. DFT calculation for enhanced MOR performance. a,b) Free energy changes for desorption of CO\* (a) and oxidation of CO\* to COOH (b) on pure Pt (black),  $MoO_x$ -Pt (red), and  $YO_x/MoO_x$ -Pt (blue) surfaces. c,d) Adsorption strategies for CO\* and COOH\* on pure Pt (c) and  $YO_x/MoO_x$ -Pt ( $MoO_x$ )-decorated Pt (d) surfaces. e) Free energy diagram for MOR on  $YO_x/MoO_x$ -Pt surface. The optimized atomic geometries of the intermediates are shown as insets. The light gray, cyan, violet, gray, red, and white spheres represent Pt, Y, Mo, C, O, and H atoms, respectively.

values further confirm that the  $YO_x/MoO_x$  co-decoration can relieve the CO\* poisoning during the EOR process (Figure S32, Supporting Information). After 2000 consecutive cycles, the activity retention obeys the following orders: 22% YOx/MoOx-Pt (57.8%) > 5% MoO<sub>x</sub>-Pt (51.0%) >Pt/C (36.9%) (Figure S33, Supporting Information). The 22% YO<sub>x</sub>/MoO<sub>x</sub>-Pt shows the best stability by showing a high mass activity of 0.94 A mg<sub>Pt</sub><sup>-1</sup> after 2000 cycles (Figure 5c), suggesting that the YO<sub>x</sub> decoration also plays a dominant role in boosting the stability toward EOR. Finally, both EGOR and GOR exhibit the trend in current densities similar to MOR or EOR (Figure S34, Supporting Information). The specific and mass activities for EGOR of 22% YOx/MoOx-Pt are 2.58 and 3.29 times higher than those of the commercial Pt/C, respectively (Figure 5d). In terms of GOR, the 22% YO<sub>x</sub>/MoO<sub>x</sub>-Pt also delivers the highest electrooxidation activity, with a specific activity of 1.05 mA cm<sup>-2</sup> and a mass activity of 0.66 A mg<sub>Pt</sub><sup>-1</sup>, respectively (Figure 5e; Table S5, Supporting Information). The in situ FTIR results further reveal that the YO<sub>x</sub>/MoO<sub>x</sub>-Pt catalyst can efficiently break the C-C bond of ethanol, ethylene glycol, and glycerol, and even can oxidize them to CO<sub>2</sub> (Figure S35, Supporting Information). The above results collectively demonstrate that ultrathin YO<sub>x</sub>/ MoO<sub>x</sub>-Pt NWs possess the enhanced electrocatalytic activity toward electro-oxidation reaction of various liquid alcohols with the optimized 22% YO<sub>x</sub>/MoO<sub>x</sub>-Pt being the best.

#### 3. Conclusions

Using the ultrathin YOx/MoOx-Pt NWs as a catalyst model, we have successfully addressed the intermediate poisoning issue via a unique decoupling mechanism, which is different from the classic bifunctional mechanism. A series of ultrathin YO<sub>x</sub>/MoO<sub>x</sub>–Pt NWs with adjustable surface-decorating amount show the low onset potential and high catalytic activities as well as the superior stability toward MOR. To be more specific, the optimized 22% YO<sub>x</sub>/MoO<sub>x</sub>-Pt shows the highest specific activity of 3.35 mA cm<sup>-2</sup> and the mass activity of 2.10 A mg<sub>Pt</sub><sup>-1</sup>. The in situ FTIR and CO-stripping results reveal that the decoration of YOx/MoOx can induce higher anti-CO poisoning ability. The enhanced electrocatalytic properties of YO<sub>x</sub>/MoO<sub>x</sub>-Pt NWs can be attributed to the high affinity of Y and Mo to oxygen, which allows the anchoring of COOH\* to the surface through both the carbon and oxygen atoms. Due to the higher oxygen affinity of Mo and Y compared with Pt, the free energies of CO\* and COOH\* can be decoupled on the YO<sub>x</sub>/ MoO<sub>x</sub>-Pt surfaces, but not on the pure Pt surface. The proposed decoupling mechanism not only mitigates the poisoning problem of the reaction intermediates toward MOR, but also demonstrates a general strategy to boost electrocatalytic performance of other liquid polyalcohols, such as ethanol, ethylene glycol, and glycerol.

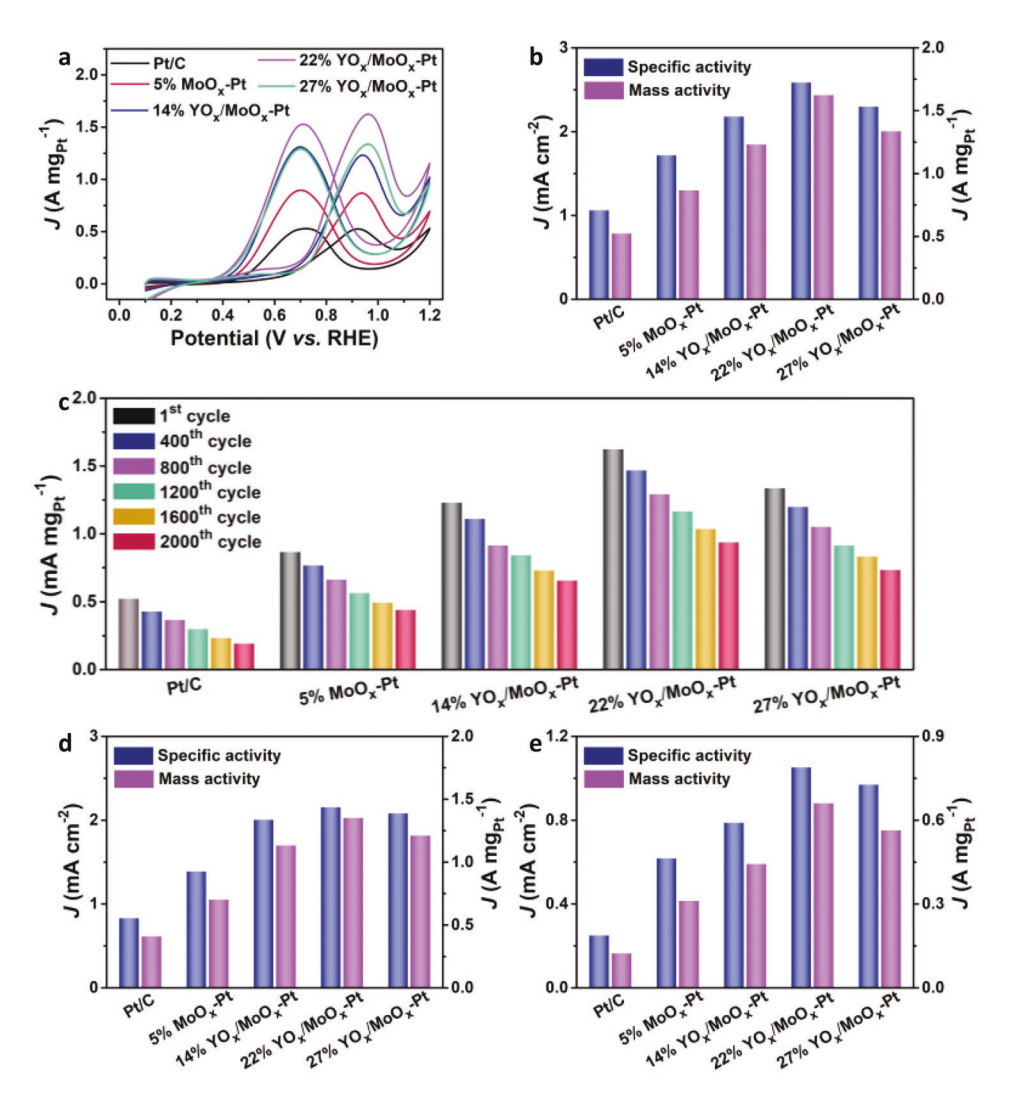


Figure 5. Electro-oxidation performance of polyalcohols on different catalysts. a) Pt mass-normalized EOR, b) comparison on the specific activities and mass activities toward EOR, and c) the mass activities toward EOR after different scan cycles. d,e) Comparison on the specific activities and mass activities toward EGOR (d) and GOR (e).

# **Supporting Information**

Supporting Information is available from the Wiley Online Library or from the author.

## **Acknowledgements**

M.L., Z.Z., and W.Z. contributed equally to this work. This study was financially supported by the Beijing Natural Science Foundation (Grant No. JQ18005), the National Science Fund for Distinguished Young Scholars (Grant No. 52025133), the Tencent Foundation through the XPLORER PRIZE, the National Key R&D Program of China (Program No. 2017YFA0206701), the National Natural Science Foundation of China (Grant Nos. 22002003, 51871078, and 52071119), BIC-ESAT funding and the China Postdoctoral Science Foundation (Grant No. 2020M670020). The work at California State University Northridge was supported by the US National Science Foundation (Grant No. DMR1828019).

#### **Conflict of Interest**

The authors declare no conflict of interest.

#### **Data Availability Statement**

Research data are not shared.

### **Keywords**

decoupling mechanism, electrocatalysis, methanol oxidation reaction, surface decoration, ultrathin nanowires

Received: May 18, 2021 Revised: June 28, 2021 Published online: August 22, 2021



www.advancedsciencenews.com



www.advmat.de

- [1] N. Kakati, J. Maiti, S. H. Lee, S. H. Jee, B. Viswanathan, Y. S. Yoon, Chem. Rev. 2014, 114, 12397.
- [2] M. Li, Z. Zhao, Z. Xia, M. Luo, Q. Zhang, Y. Qin, L. Tao, K. Yin, Y. Chao, L. Gu, W. Yang, Y. Yu, G. Lu, S. Guo, Angew. Chem., Int. Ed. 2021, 60, 8243.
- [3] Z. W. Seh, J. Kibsgaard, C. F. Dickens, I. Chorkendorff, J. K. Nørskov, T. F. Jaramillo, Science 2017, 355, eaad4998.
- [4] A. A. Dubale, Y. Zheng, H. Wang, R. Hübner, Y. Li, J. Yang, J. Zhang, N. K. Sethi, L. He, Z. Zheng, W. Liu, Angew. Chem., Int. Ed. 2020, 59, 13891.
- [5] L. Tao, Z. Xia, Q. Zhang, Y. Sun, M. Li, K. Yin, L. Gu, S. Guo, Sci. Bull. 2021, 66, 44.
- [6] X. Cui, P. Xiao, J. Wang, M. Zhou, W. Guo, Y. Yang, Y. He, Z. Wang, Y. Yang, Y. Zhang, Z. Lin, Angew. Chem., Int. Ed. 2017, 56, 4488.
- [7] X. Wang, S. Xi, W. S. V. Lee, P. Huang, P. Cui, L. Zhao, W. Hao, X. Zhao, Z. Wang, H. Wu, H. Wang, C. Diao, A. Borgna, Y. Du, Z. G. Yu, S. Pennycook, J. Xue, *Nat. Commun.* **2020**, *11*, 4647.
- [8] C. Li, X. Chen, L. Zhang, S. Yan, A. Sharma, B. Zhao, A. Kumbhar, G. Zhou, J. Fang, Angew. Chem., Int. Ed. 2021, 60, 7675.
- [9] S. H. HanH. M. LiuP. ChenJ. X. Jiang, Y. Chen, Adv. Energy Mater. 2018, 8, 1801326.
- [10] J. T. L. Gamler, H. M. Ashberry, S. E. Skrabalak, K. M. Koczkur, Adv. Mater. 2018, 30, 1801563.
- [11] N. Ramaswamy, S. Mukerjee, Chem. Rev. 2019, 119, 11945.
- [12] L. Xiong, Z. Sun, X. Zhang, L. Zhao, P. Huang, X. Chen, H. Jin, H. Sun, Y. Lian, Z. Deng, M. H. Rümmerli, W. Yin, D. Zhang, S. Wang, Y. Peng, Nat. Commun. 2019, 10, 3782.
- [13] J. M. Kim, J. H. Kim, J. Kim, Y. Lim, Y. Kim, A. Alam, J. Lee, H. Ju, H. C. Ham, J. Y. Kim, Adv. Mater. 2020, 32, 2002210.
- [14] S. Y. Ma, H. H. Li, B. C. Hu, X. Cheng, Q. Q. Du, S. H. Yu, J. Am. Chem. Soc. 2017, 139, 5890.
- [15] Y. Yang, M. Luo, W. Zhang, Y. Sun, X. Chen, S. Guo, Chem 2018, 4, 2054.
- [16] R. Riza, B. R. Cuenya, ACS Energy Lett. 2019, 4, 1484.
- [17] K. Liu, W. Wang, P. Guo, J. Ye, Y. Wang, P. Li, Z. Lyu, Y. Geng, M. Liu, S. Xie, Adv. Funct. Mater. 2019, 29, 1806300.
- [18] W. Li, D. Wang, Y. Zhang, L. Tao, T. Wang, Y. Zou, Y. Wang, R. Chen, S. Wang, Adv. Mater. 2020, 32, 1907879.
- [19] Z. Zhang, Z. Luo, B. Chen, C. Wei, J. Zhao, J. Chen, X. Zhang, Z. Lai, Z. Fan, C. Tan, M. Zhao, Q. Lu, B. Li, Y. Zong, C. Yan, G. Wang, Z. J. Xu, H. Zhang, Adv. Mater. 2016, 28, 8712.
- [20] Q. Feng, S. Zhao, D. He, S. Tian, L. Gu, X. Wen, C. Chen, Q. Peng, D. Wang, Y. Li, J. Am. Chem. Soc. 2018, 140, 2773.
- [21] X. Cui, Z. Zhang, Y. Gong, F. Saleem, B. Chen, Y. Du, Z. Lai, N. Yang, B. Li, L. Gu, H. Zhang, CCS Chem. 2020, 2, 24.
- [22] W. Lei, M. Li, L. He, X. Meng, Z. Mu, Y. Yu, F. M. Ross, W. Yang, Nano Res. 2020, 13, 638.
- [23] H. Li, Y. Han, H. Zhao, W. Qi, D. Zhang, Y. Yu, W. Cai, S. Li, J. Lai, B. Huang, L. Wang, Nat. Commun. 2020, 11, 5437.
- [24] M. Li, Z. Zhao, Z. Xia, Y. Yang, M. Luo, Y. Huang, Y. Sun, Y. Chao, W. Yang, W. Yang, Y. Yu, G. Lu, S. Guo, ACS Catal. 2020, 10, 3018.
- [25] Y. Zheng, J. Yang, X. Lu, H. Wang, A. A. Dubale, Y. Li, Z. Jin, D. Lou, N. K. Sethi, Y. Ye, J. Zhou, Y. Sun, Z. Zheng, W. Liu, Adv. Energy Mater. 2021, 11, 2002276.
- [26] J. Yang, R. Hübner, J. Zhang, H. Wan, Y. Zheng, H. Wang, H. Qi, L. He, Y. Li, A. A. Dubale, Y. Sun, Y. Liu, D. Peng, Y. Meng, Z. Zheng, J. Rossmeisl, W. Liu, Angew. Chem., Int. Ed. 2021, 60, 9590.
- [27] J. Mao, W. Chen, D. He, J. Wan, J. Pei, J. Dong, Y. Wang, P. An, Z. Jin, W. Xing, H. Tang, Z. Zhuang, X. Liang, Y. Huang, G. Zhou, L. Wang, D. Wang, Y. Li, Sci. Adv. 2017, 3, e1603068.

- [28] K. Jiang, D. Zhao, S. Guo, X. Zhang, X. Zhu, J. Guo, G. Lu, X. Huang, Sci. Adv. 2017, 3, e1601705.
- [29] C. Li, B. Huang, M. Luo, Y. Qin, Y. Sun, Y. Li, Y. Yang, D. Wu, M. Li, S. Guo, Appl. Catal. B 2019, 256, 117828.
- [30] L. Gao, X. Li, Z. Yao, H. Bai, Y. Lu, C. Ma, S. Lu, Z. Peng, J. Yang, A. Pan, H. Huang, J. Am. Chem. Soc. 2019, 141, 18083.
- [31] H. Xu, H. Shang, C. Wang, Y. Du, Adv. Funct. Mater. 2020, 30, 2000793.
- [32] Y. Zhu, X. Zhu, L. Bu, Q. Shao, Y. Li, Z. Hu, C. T. Chen, C. W. Pao, S. Yang, X. Huang, Adv. Funct. Mater. 2020, 30, 2004310.
- [33] M. Li, F. Tian, T. Lin, L. Tao, X. Guo, Y. Chao, Z. Guo, Q. Zhang, L. Gu, W. Yang, Y. Yu, S. Guo, Small Methods 2021, 5, 2100154.
- [34] Y. Wang, Y. Yuan, H. Huang, Chin. J. Chem. 2021, 39, 1389.
- [35] L. Zhang, H. Zhao, S. Xu, Q. Liu, T. Li, Y. Luo, S. Gao, X. Shi, A. M. Asiri, X. Sun, Small Struct. 2021, 2, 2000048.
- [36] Z. Cui, H. Chen, M. Zhao, D. Marshall, Y. Yu, H. Abruña, F. J. DiSalvo, J. Am. Chem. Soc. 2014, 136, 10206.
- [37] F. Kong, C. Du, J. Ye, G. Chen, L. Du, G. Yin, ACS Catal. 2017, 7, 7923
- [38] L. Huang, X. Zhang, Q. Wang, Y. Han, Y. Fang, S. Dong, J. Am. Chem. Soc. 2018, 140, 1142.
- [39] Q. Chang, S. Kattel, X. Li, Z. Liang, B. M. Tackett, S. R. Denny, P. Zhang, D. Su, J. G. Chen, Z. Chen, ACS Catal. 2019, 9, 7618.
- [40] L. Huang, C. Y. Zheng, B. Shen, C. A. Mirkin, Adv. Mater. 2020, 32, 2002849.
- [41] N. Guo, H. Xue, A. Bao, Z. Wang, J. Sun, T. Song, X. Ge, W. Zhang, K. Huang, F. He, Q. Wang, Angew. Chem., Int. Ed. 2020, 59, 13778.
- [42] Y. Zhang, M. Janyasupab, C. W. Liu, X. Li, J. Xu, C. C. Liu, Adv. Funct. Mater. 2012, 22, 3570.
- [43] K. Wang, H. Du, R. Sriphathoorat, P. K. Shen, Adv. Mater. 2018, 30, 1804074.
- [44] W. Zhang, Y. Yang, B. Huang, F. Lv, K. Wang, N. Li, M. Luo, Y. Chao, Y. Li, Y. Sun, Z. Xu, Y. Qin, W. Yang, J. Zhou, Y. Du, D. Su, S. Guo, Adv. Mater. 2019, 31, 1805833.
- [45] W. Wang, X. Chen, X. Zhang, J. Ye, F. Xue, C. Zhen, X. Liao, H. Li, P. Li, M. Liu, Q. Kuang, Z. Xie, S. Xie, Nano Energy 2020, 71, 104623.
- [46] S. Zhang, S. E. Saji, Z. Yin, H. Zhang, Y. Du, C. H. Yan, Adv. Mater. 2021, 33, 2005988.
- [47] J. E. Sulaiman, S. Zhu, Z. Xing, Q. Chang, M. Shao, ACS Catal. 2017. 7, 5134.
- [48] N. Erini, V. Beermann, M. Gocyla, M. Gliech, M. Heggen, R. E. Dunin-Borkowski, P. Strasser, Angew. Chem., Int. Ed. 2017, 56, 6533
- [49] G. Q. Lu, S. G. Sun, L. R. Cai, S. P. Chen, Z. W. Tian, K. K. Shiu, Langmuir 2000, 16, 778.
- [50] J. Chang, L. Feng, K. Jiang, H. Xue, W. B. Cai, C. Liu, W. Xing, J. Mater. Chem. A 2016, 4, 18607.
- [51] Y. X. Chen, A. Miki, S. Ye, H. Sakai, M. Osawa, J. Am. Chem. Soc. 2003, 125, 3680.
- [52] Y. Y. Yang, J. Ren, Q. X. Li, Z. Y. Zhou, S. G. Sun, W. B. Cai, ACS Catal. 2014, 4, 798.
- [53] W. Huang, X. Y. Ma, H. Wang, R. Feng, J. Zhou, P. N. Duchesne, P. Zhang, F. Chen, N. Han, F. Zhao, J. Zhou, W. B. Cai, Y. Li, Adv. Mater. 2017, 29, 1703057.
- [54] M. E. Scofield, C. Koenigsmann, L. Wang, H. Liu, S. S. Wong, Energy Environ. Sci. 2015. 8, 350.
- [55] Z. Qi, C. Xiao, C. Liu, T. W. Goh, L. Zhou, R. Maligal-Ganesh, Y. Pei, X. Li, L. A. Curtiss, W. Huang, J. Am. Chem. Soc. 2017, 139, 4762.
- [56] H. Liu, C. Song, L. Zhang, J. Zhang, H. Wang, D. P. Wilkinson, J. Power Sources 2006, 15, 95.
- [57] V. Mazumder, Y. Lee, S. Sun, Adv. Funct. Mater. 2010, 20, 1224.